


# Concomitant formation of a pseudogap with the $\beta$ -to- $\beta'$ structural phase transition in melt-quenched $\text{As}_2\text{Te}_3$

Jeremy Dion , Collin Tower , and Maureen Reedyk *Department of Physics, Brock University, St. Catharines, Ontario, Canada L2S 3A1*

(Received 14 January 2022; revised 8 July 2022; accepted 11 July 2022; published 1 August 2022)

$\text{As}_2\text{Te}_3$  is a chalcogenide with many polymorphic phases. Of current interest are the  $\beta$  and  $\beta'$  phases which have been investigated primarily in the context of their close relationship to the isostructural topological insulator  $\text{Bi}_2\text{Te}_3$ . The  $\beta$ -to- $\beta'$  phase transition of  $\text{As}_2\text{Te}_3$  exhibits a large anomaly in the resistivity that has remained unexplained. In this work we have measured the electronic transport properties of this phase transition in melt-quenched  $\text{As}_2\text{Te}_3$  via dc resistivity and infrared reflectivity measurements. A sigmoidal fit has been used to describe the general behavior of the resistivity curves over a wide temperature range in order to characterize how hysteresis affects the phase transition anomaly. The optical measurements have identified the formation of a concomitant pseudogap of magnitude  $\approx 100$  meV affecting approximately 25% of the carriers. Charge density wave order is compatible with the formation of a partial gap as well as the observation of thermal hysteresis, suggesting it could be responsible for the  $\beta$ - $\beta'$  transition in melt-quenched  $\text{As}_2\text{Te}_3$ .

DOI: [10.1103/PhysRevB.106.075104](https://doi.org/10.1103/PhysRevB.106.075104)

## I. INTRODUCTION

The chalcogenides are a family of layered compounds that have been the subject of considerable interest. The crystalline phases of these materials are found to exhibit exotic properties including strange metallicity [1], the formation of charge [2] and spin density waves [3], and superconducting [4] and topological insulating phases [5], typically under pressure and/or with doping. One of the earliest chalcogenides discovered to combine superconductivity and charge density wave order was quasi-low-dimensional  $\text{NbSe}_2$  [6]. More recently the rare-earth metal tritellurides have garnered significant interest. In addition to charge density wave (CDW) and superconducting orders these low-dimensional materials such as  $\text{ErTe}_3$ ,  $\text{TmTe}_3$ , and  $\text{HoTe}_3$  [7,8] exhibit spin density wave states and other quantum collective behavior [9].

The sesquichalcogenides which have the composition  $Pn_2Ch_3$  where  $Pn$  is a pnictogen such as As, Sb, or Bi and  $Ch$  is a chalcogen such as S, Se, or Te [10] are another notable group of interest. Topological insulator  $\text{Bi}_2\text{Te}_3$  is a well-known member of this family which becomes superconducting with doping [11–13]. Other members of this family such as  $\text{Sb}_2\text{Te}_3$ ,  $\text{Sb}_2\text{Se}_3$ , and  $\text{Bi}_2\text{Se}_3$  also exhibit exotic states such as topological insulation [11–13] and, upon doping, ferromagnetism [14,15].

$\text{As}_2\text{Te}_3$  is a layered sesquichalcogenide that has  $\alpha$ ,  $\beta$ , and  $\beta'$  polymorphic phases [16].  $\alpha$ - $\text{As}_2\text{Te}_3$  is monoclinic with space group  $C2/m$  [16] and is a typical semiconductor with resistivity decreasing with increasing temperature [17].  $\beta$ - $\text{As}_2\text{Te}_3$  can be produced from  $\alpha$ - $\text{As}_2\text{Te}_3$  via a rapid melt quench [16]. Formed in this manner,  $\beta$ - $\text{As}_2\text{Te}_3$  is a metastable phase [16].  $\beta$ - $\text{As}_2\text{Te}_3$  exhibits significantly different electronic properties when compared to  $\alpha$ - $\text{As}_2\text{Te}_3$ , with the former showing metallic character with significantly lower resistivity [18].

$\beta$ - $\text{As}_2\text{Te}_3$  has the same rhombohedral space group  $R\bar{3}m$  as  $\text{Bi}_2\text{Te}_3$ ; however,  $\beta$ - $\text{As}_2\text{Te}_3$  has not been nearly as extensively studied experimentally, with the focus primarily on optimizing its properties for thermoelectric applications [16,18–20]. Theoretical investigations have, however, predicted that  $\beta$ - $\text{As}_2\text{Te}_3$  is an exotic metal that will undergo a quantum topological phase transition under pressure [21–23].

Upon lowering temperature,  $\beta$ - $\text{As}_2\text{Te}_3$  undergoes a reversible first-order structural phase transition to monoclinic (space group  $P2_1/m$ )  $\beta'$ - $\text{As}_2\text{Te}_3$  near 200 K [16]. Accompanying this transition is an anomaly in the resistivity which has been speculated to be caused by internal strain from the crystal structure change [24]; however, the underlying mechanism for the  $\beta$  to  $\beta'$  phase change is still unknown.

Herein we examine the resistivity and infrared reflectivity of melt-quenched sesquichalcogenide  $\text{As}_2\text{Te}_3$ . The  $\beta$ - $\text{As}_2\text{Te}_3$  formed is characterized by a high, but metallic resistivity. The  $\beta$ -to- $\beta'$  transition is found to show temperature hysteresis and is accompanied by the formation of a partial gap. These observations are evidence that  $\beta$ - $\text{As}_2\text{Te}_3$  possesses nontrivial electron interactions at low temperature which we suggest may be the result of the formation of a charge density wave ordered state.

## II. EXPERIMENT

We have investigated  $\beta$ - $\text{As}_2\text{Te}_3$  using techniques including infrared reflectivity, dc resistivity, and powder x-ray diffraction (PXRD) with a focus primarily on the  $\beta$ -to- $\beta'$  phase transition.

To synthesize samples, polycrystalline  $\alpha$ - $\text{As}_2\text{Te}_3$  (Alfa Aesar, 99.999%) was ground to a powder, placed inside a quartz ampoule, and evacuated of air to a pressure of  $\approx 10^{-6}$  torr. The ampoule was then sealed and placed in a single-zone furnace and heated to 850 °C where it was soaked for 2 h. The

sample was removed from the oven and rapidly quenched in a salt/ice water bath adjacent to the oven.

X-ray diffraction (XRD) measurements were performed using a Rigaku x-ray diffractometer. Samples were ground into a fine powder and Bragg-Brentano focusing was used to acquire the PXRD pattern. The resulting PXRD patterns were analyzed with the Rigaku PDXL software utilizing crystallographic models from known literature for both the  $\alpha$  and  $\beta$  phases of  $\text{As}_2\text{Te}_3$  [16] and tellurium from the Crystallography Open Database [25,26].

dc-resistivity measurements were carried out using van der Pauw geometry in an evacuated chamber at temperatures in the range of 20–300 K. Silver paint was used to attach gold wires to the sample. The samples were mounted to a cold finger with Apiezon N grease for thermal contact and a temperature sensor was attached directly to the sample mount. The thickness of the sample was taken into account to obtain the temperature-dependent absolute resistivity from the van der Pauw theory [27].

Optical reflectivity measurements were carried out on a polished sample piece using a Bruker Michelson Interferometer and cold-finger cryostat at 30 different temperatures between 85 K and room temperature in the midinfrared (MIR). Absolute reflectivity was determined by using an *in situ* gold deposition technique [28]. These measurements were supplemented by far-infrared (FIR) and near-infrared measurements at select temperatures which were interpolated for intermediate temperatures in order to guide the low- and high-wavenumber behavior of the model fits to the MIR reflectance.

### III. RESULTS

#### A. X-ray diffraction

Figure 1 depicts the XRD patterns for the source  $\alpha - \text{As}_2\text{Te}_3$  and the melt-quenched  $\beta - \text{As}_2\text{Te}_3$ . The XRD patterns acquired closely match the literature in which secondary methods such as neutron diffraction were used to verify phase purity [16] with the exception of a peak at  $39^\circ$  attributed to a potential tellurium excess which is common in tellurium-containing sesquichalcogenides [29].

Rietveld analysis of the XRD patterns for  $\beta - \text{As}_2\text{Te}_3$  was performed to confirm the formation of majority  $\beta$  phase. We investigated  $\alpha - \text{As}_2\text{Te}_3$ ,  $\beta - \text{As}_2\text{Te}_3$ , and Te with our model and acquired percent compositions of 1.8%, 93.9%, and 4.3%, respectively, and a weighted profile residual value ( $R_{WP}$ ) of 3.35%. Note that  $\alpha - \text{As}_2\text{Te}_3$  did not appreciably change the fit quality upon removal, and due to the overlap of a number of peaks between it,  $\beta - \text{As}_2\text{Te}_3$  and Te, it is possible it is overquantified. Texturing caused by preferred orientation of the powder can cause relative intensities of peaks to vary. From the analysis we estimate that there is a significant preferential orientation towards the  $c$  axis as a result of the layered nature of the crystal structure.

#### B. dc resistivity

Figure 2(a) shows the resistivity of melt-quenched  $\beta - \text{As}_2\text{Te}_3$  as a function of temperature with warming and cooling curves showing thermal hysteresis. The  $\beta \rightarrow \beta'$  phase

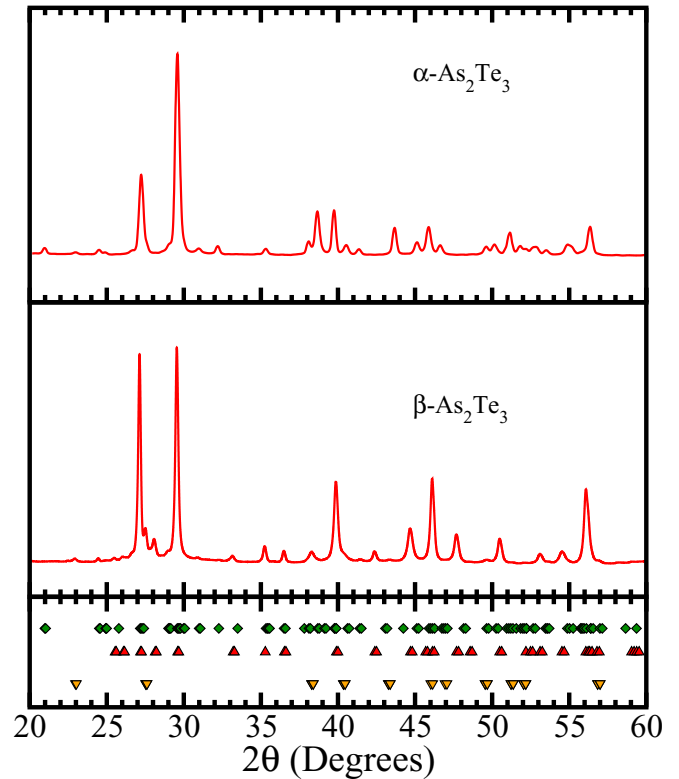


FIG. 1. XRD patterns of  $\alpha$ - and  $\beta - \text{As}_2\text{Te}_3$ . Patterns were investigated by Rietveld analysis using literature CIF files [16,25,26]. Calculated peak positions are represented in the lower panel with diamonds (green), rightside-up (red) triangles, and inverted (yellow) triangles representing  $\alpha - \text{As}_2\text{Te}_3$ ,  $\beta - \text{As}_2\text{Te}_3$ , and tellurium peaks, respectively. For clarity, only calculated peaks with intensity greater than 0.5% max intensity are indicated.

transition appears prominently in the resistivity curves below 200 K as expected. The derivative of the resistivity with respect to temperature  $d(\rho)/d(T)$  was evaluated for both warming and cooling [see Fig. 2(a), inset], with the sharp minimum characterizing the temperature of the  $\beta$ -to- $\beta'$  phase transition. A hysteresis of approximately 7 K is observed between the measured value of the transition temperature upon warming and cooling suggestive of a first-order phase transition.

The room temperature resistivity value measured in this work for melt-quenched  $\text{As}_2\text{Te}_3$  of  $\approx 3.25 \times 10^{-5} \Omega \text{m}$  is of the order of other related  $R\bar{3}m$  space group sesquichalcogenides. For example, *ab*-plane  $\text{Bi}_2\text{Te}_3$  exhibited a room temperature resistivity value of  $2 \times 10^{-5} \Omega \text{m}$  [30] while that of  $\text{Bi}_2\text{Se}_3$  was  $\approx 6 \times 10^{-5} \Omega \text{m}$  [31]. Previous work on pressed  $\beta - \text{As}_2\text{Te}_3$  yielded room temperature resistivity values of  $2.2 \times 10^{-5} \Omega \text{m}$  and  $1.2 \times 10^{-5} \Omega \text{m}$  for samples cut parallel and perpendicular to the pressing direction, respectively [24].

#### C. Infrared reflectivity

Figure 3 shows the experimental FIR and MIR reflectance at selected temperatures (solid curves). At temperatures above the  $\beta$ -to- $\beta'$  phase transition (290 and 250 K) the reflectance

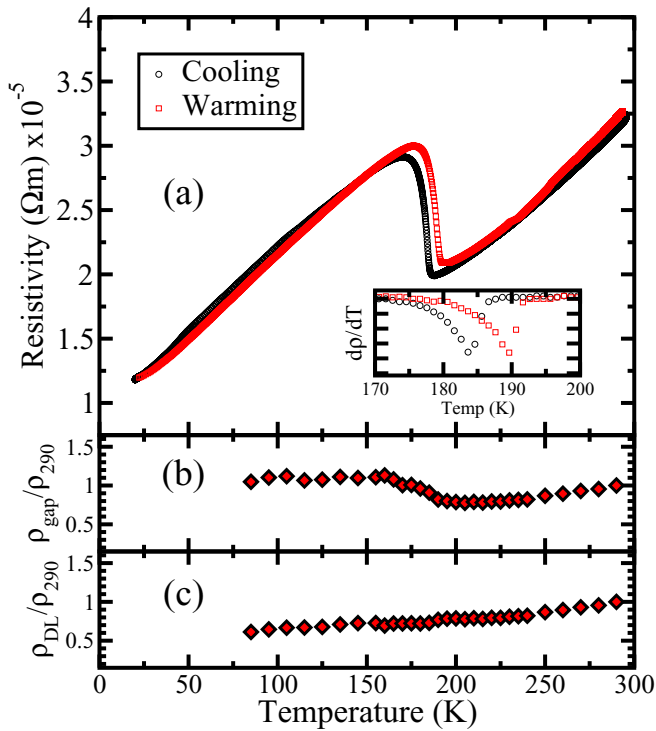


FIG. 2. (a) dc resistivity of melt-quenched  $\text{As}_2\text{Te}_3$  upon warming (square) and cooling (circle). Hysteresis between warming and cooling measurements is observed. The inset shows  $d\rho/dT$  with the minimum used to characterize the  $\beta$ -to- $\beta'$  transition temperature. (b) and (c) depict the normalized resistivity acquired from optical reflectivity fits to the gapped-Drude and Drude-Lorentz models, respectively.

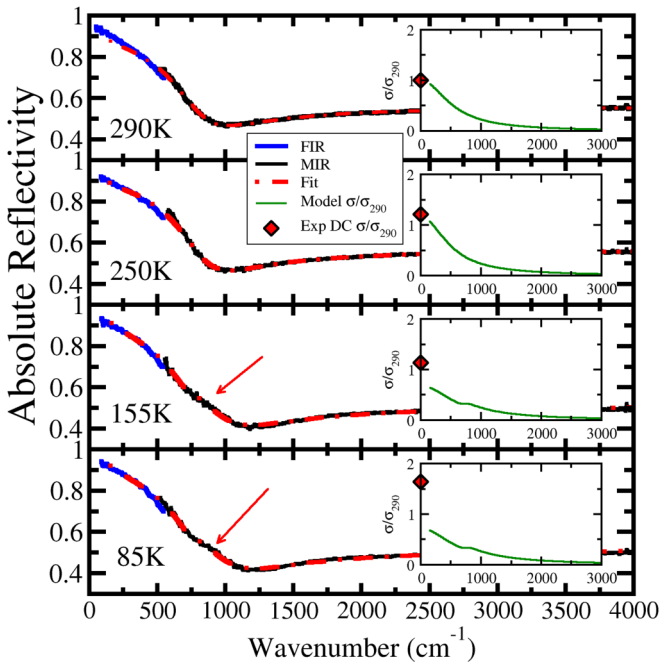


FIG. 3. Experimental FIR and MIR reflectance at selected temperatures (solid curves) with model fits (dashed curves). See text for details. Insets: model of real frequency-dependent optical and experimental dc conductivity normalized to 290 K dc conductivity.

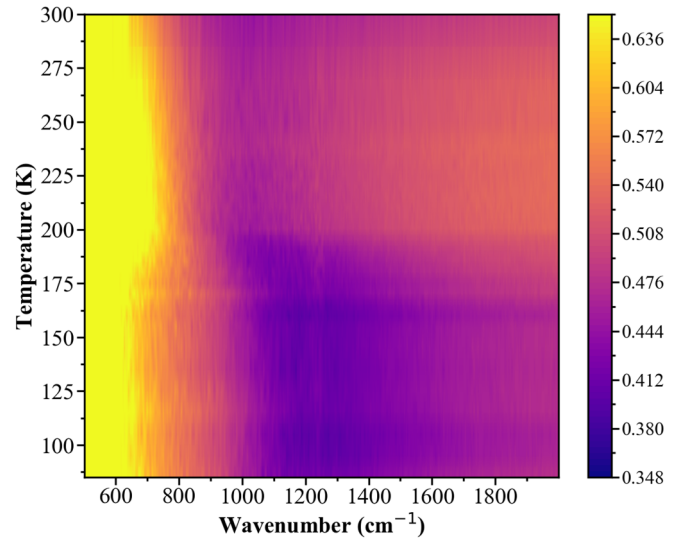


FIG. 4. A color map of the MIR reflectivity in the region of the Drude response as a function of temperature and wavenumber.

is Drude-like with a plasma edge and well-defined minimum. The reflectance data was fit to the Drude model (dashed curves in Fig. 3) and a good quality fit was obtained with no need to include any additional Lorentz oscillators. Figure S1 in the Supplemental Material gives the room temperature reflectance and the model fit over a wider wavenumber range extending into the near infrared [32]. At higher wavenumber it is clear that a complete description would require additional oscillators to represent interband transitions. The reflectivity can be written in terms of the dielectric function according to

$$R = \left| \frac{1 - \sqrt{\epsilon(\omega)}}{1 + \sqrt{\epsilon(\omega)}} \right|^2, \quad (1)$$

where the Drude model dielectric function is given by

$$\epsilon(\omega) = \epsilon_\infty - \frac{\omega_p^2}{\omega^2 + i\omega\gamma}. \quad (2)$$

Here  $\epsilon_\infty$  represents the high-frequency permittivity,  $\omega_p$  refers to the unscreened plasma frequency—its square being proportional to the carrier density—and  $\gamma$  denotes the scattering rate.

To more readily visualize changes occurring with temperature, Fig. 4 shows a color map of the reflectivity in the vicinity of the plasma minimum formed from the 30 measurements of MIR reflectance obtained between 85 K and room temperature. The plasma edge (bright) and its minimum (dark) can be viewed in the region below approximately  $1200 \text{ cm}^{-1}$ . Note the distinct changes that occur below the  $\beta$ -to- $\beta'$  phase transition near 190 K. The constant reflectance beyond the plasma edge drops approximately 3% as is evident by the clear color delineation above and below 190 K and a new feature emerges near the plasma edge between 700 and  $1000 \text{ cm}^{-1}$  (marked by an arrow in Fig. 3).

All model fits were performed using the REFFIT public domain, optical analysis software [33]. As discussed above, in the  $\beta$  phase ( $T > 190 \text{ K}$ ) a simple Drude fit is sufficient but upon entering the  $\beta'$  —  $\text{As}_2\text{Te}_3$  regime a revised model is

required to fit the data. Two models were investigated to fit to this low temperature regime: a “gapped” Drude using the gapped Drude function in REFFIT [34] and a more conventional Drude + Lorentz oscillator model. Both models reproduce the reflectivity well and as such similar conclusions are drawn from both models in the region of the experimental data.

### 1. Gapped model

The gapped Drude model is given by the frequency-dependent dielectric function:

$$\epsilon(\omega) = \epsilon_{\text{real}}(\omega) + i \frac{4\pi\sigma_{\text{gap}}(\omega)}{\omega} + A\delta(\omega), \quad (3)$$

where  $\epsilon_{\text{real}}(\omega)$  is the real part of the dielectric function and  $\sigma_{\text{gap}}(\omega)$  is a modification of the real Drude conductivity

$$\sigma_{\text{Drude}}(\omega) = \frac{\omega_p^2\gamma}{4\pi(\gamma^2 + \omega^2)} \quad (4)$$

by multiplying it with  $\Gamma(\omega)$ , a smoothed step function, as follows:

$$\sigma_{\text{gap}}(\omega) = \Gamma(\omega)\sigma_{\text{Drude}}(\omega), \quad (5)$$

where

$$\Gamma(\omega) = 1 - \frac{\xi_0}{2} \left[ 1 - \tanh\left(\frac{\omega - \omega_g}{2\gamma_g}\right) \right]. \quad (6)$$

Here  $\omega_g$  represents the magnitude of the gap,  $\gamma_g$  represents the gap broadening, and the gapping fraction  $\xi_0$  represents the fractional carriers removed [34]. In Eq. (3),  $A\delta(\omega)$ , where  $\delta(\omega)$  is the Dirac delta, accounts for the loss of spectral weight due to the gap formation in order to maintain Kramers-Kronig consistency by keeping total spectral weight constant [34]. The gapped spectral weight is thus recovered as a sharp mode at the origin. In practice the spectral weight may be recovered at energies higher or lower than the experimental spectral range. Note that a similar approach was used to model pseudogap formation in  $\text{YBa}_2\text{Cu}_3\text{O}_{6+x}$  [35].

The temperature dependence of the Drude parameters and gapping fraction obtained from the model fits can be found in Fig. 5. As temperature increases, and a transition from the  $\beta'$  to the  $\beta$  phase takes place, clear changes in the optical parameters occur.  $\epsilon_\infty$  undergoes an increase from  $\approx 37$  to  $\approx 50$ . Likewise  $\gamma$  shifts from a value of  $600 \text{ cm}^{-1}$  (74 meV) in the  $\beta'$  phase to  $480 \text{ cm}^{-1}$  (60 meV) at 200 K in the  $\beta$  phase, followed by a linear increase to around  $580 \text{ cm}^{-1}$  (72 meV) at 300 K.

In this model the unscreened plasma frequency  $\omega_p$  exhibits only a weak temperature dependence since the carriers removed are accounted for by the gapping fraction. The Drude parameters of the gapped model are constant with temperature up until approximately 175 K where  $\xi_0$  decreases as the material approaches the  $\beta'$ - $\beta$  phase transition temperature. The magnitude of the gap was found to be  $758 \pm 9 \text{ cm}^{-1}$  ( $94 \pm 1 \text{ meV}$ ), with a broadening of  $39 \pm 4 \text{ cm}^{-1}$  ( $4.8 \pm 0.5 \text{ meV}$ ).

The inset panels in Fig. 3 compare the experimental normalized dc conductivity acquired via the resistivity at selected

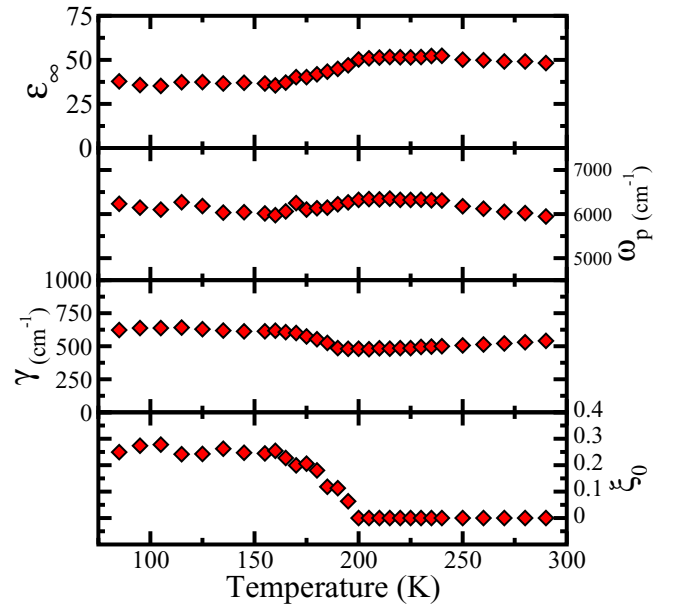


FIG. 5. Model parameters acquired from fitting the experimental reflectivity spectra collected at each temperature.

temperatures, to the normalized real frequency-dependent optical conductivity obtained from the fits to the reflectance described above. The loss in spectral weight due to the formation of the gap, that has been modeled to shift to a sharp mode at the origin, is clearly evident upon transitioning to the  $\beta'$  phase as the normalized dc conductivity no longer matches the zero-wavenumber limit of the real optical conductivity.

### 2. Drude-Lorentz model

As is common for materials exhibiting two electronic subsystems (see, e.g., [36–38]), in the Drude-Lorentz treatment we have modeled the reflectivity below the  $\beta$ - $\beta'$  phase transition using two Drude contributions and a Lorentz oscillator as described in the Supplemental Material [32]. The fit parameters are plotted as a function of temperature in Figs. S3 and S4 of the Supplemental Material [32]. The magnitude of the gap as given by the frequency of the Lorentz oscillator is found to be  $870 \pm 20 \text{ cm}^{-1}$  ( $108 \pm 2 \text{ meV}$ ), in reasonable agreement with the gapped model given the very different mathematical representations for the gap.

## IV. DISCUSSION

### A. dc resistivity

The dc resistivity exhibits a relatively sharp increase at the temperature of the structural phase transition from  $\beta$  to  $\beta'$ . This is suggestive of a reduced carrier density produced by a reconstruction of the Fermi surface. Similar behavior has been observed concurrent with a phase transition in other materials such as the pnictide  $\text{CaFe}_2\text{As}_2$  [39], the transition metal dichalcogenide  $\text{IrTe}_2$  [40], and the rare-earth ternary silicides  $\text{Lu}_2\text{Ir}_3\text{Si}_5$  [41] and  $\text{Er}_2\text{Ir}_3\text{Si}_5$  [42,43]. In all of these systems the resistivity anomaly has the distinctive shape of a tanh curve typically superimposed on a quasilinear background. Furthermore, hysteresis is observed between the warming and

TABLE I. Parameters obtained by fitting resistivity to Eq. (7). The warming and cooling curves from this work (first two rows) were fit using a temperature range from  $\approx 30$  K to room temperature. The last column gives the transition temperature obtained from the derivative of the resistivity data as shown in the inset in Fig. 2(a). Rows 3–5 show the results of fitting to literature data. Note that the data curve of Ref. [16] was normalized to room temperature. We have multiplied it by our room temperature resistivity to make the comparison more meaningful.

Data source	$\zeta$ ( $\Omega \text{ m/K} \times 10^{-7}$ )	$c$ ( $\Omega \text{ m} \times 10^{-6}$ )	$\kappa$ ( $\Omega \text{ m} \times 10^{-6}$ )	$\chi$ (1/K)	$T_{\beta'}$ (K)	$d\rho/dT$ min (K)
This work cooling	$1.21 \pm 0.02$	$2.77 \pm 0.04$	$6.72 \pm 0.02$	$0.17 \pm 0.02$	$181.7 \pm 0.4$	$184.5 \pm 0.5$
This work warming	$1.28 \pm 0.02$	$1.64 \pm 0.04$	$6.89 \pm 0.02$	$0.16 \pm 0.02$	$187.6 \pm 0.5$	$189.0 \pm 0.5$
Normalized melt quenched [16]	$1.42 \pm 0.05$	$6.3 \pm 0.1$	$4.57 \pm 0.04$	$0.20 \pm 0.01$	$192.8 \pm 0.1$	$190.1 \pm 0.5$
Perp. pressed warming [24]	$0.25 \pm 0.02$	$6.02 \pm 0.03$	$1.73 \pm 0.02$	$0.064 \pm 0.002$	$188.3 \pm 0.2$	$186 \pm 3$
Perp. pressed cooling [24]	$0.25 \pm 0.02$	$5.87 \pm 0.04$	$1.93 \pm 0.02$	$0.058 \pm 0.002$	$182.9 \pm 0.2$	$182 \pm 1$

cooling resistivity curves. As shown in Fig. 2(a) a clear hysteresis is observed across the  $\beta$ -to- $\beta'$  phase transition which was also remarked on by Vaney *et al.* [24].

Notably,  $\beta - \text{As}_2\text{Te}_3$  and  $\beta' - \text{As}_2\text{Te}_3$  are observed to have approximately parallel quasilinear resistivity regimes outside the region of the phase transition. To characterize the  $\beta$ -to- $\beta'$  phase transition as observed in the resistivity we fit both the warming and the cooling curves to the following phenomenological equation at temperatures from 30 to 300 K:

$$\rho(T) = c + \zeta T - \kappa \tanh[\chi(T - T_{\beta'})]. \quad (7)$$

Here  $\zeta$  and  $c$  represent the slope and level-adjust fitting parameter, respectively, of a slope invariant  $T$ -linear resistivity across a phase transition.  $\kappa$  represents the amplitude of the steplike signature of the phase transition and  $\chi$  represents its temperature broadening.  $T_{\beta'}$  represents the temperature of the phase transition. Note that in the zero temperature limit  $\tanh[\chi(T - T_{\beta'})] \rightarrow -1$  and thus  $c + \kappa$  represents the residual resistivity. The results of this analysis can be found in Table I and the fits compared to experimental data can be viewed in Fig. 6 confirming that a singular slope models the general behavior of the resistivity over a wide temperature range ( $\approx 30$  to 300 K in the warming curve).

To appreciate the effect of the synthesis method on the resistivity we also applied this model to the room temper-

ature normalized resistivity of melt-quenched  $\text{As}_2\text{Te}_3$  from Ref. [16] as well as to the ground and pressed samples of Ref. [24]. We scaled the normalized resistivity of Ref. [16] to our room temperature resistivity to facilitate comparison. The results are included in Table I. Comparing these values we note that the slope ( $\zeta$ ) is considerably greater in the melt-quenched samples than in the pressed samples, indicating that the melt-quenched samples exhibit a much stronger temperature dependence. This conclusion also holds if normalized resistivity is considered. The fractional increase in resistivity at the  $\beta$ -to- $\beta'$  phase transition relative to the room temperature resistivity in melt-quenched samples,  $\kappa/\rho_{290 \text{ K}}$ , is significantly enhanced over that in pressed samples, and is also broader (larger  $\chi$ ). The level-adjust parameter,  $c$ , is lower for the samples of this work than those in the literature. Generally Eq. (7) fit the melt-quenched samples best, with the resistivity of the ground and pressed sample measured parallel to the pressing direction deviating more strongly from  $T$ -linear behavior below the phase transition [24]. As the pressed samples exhibit anisotropy, this process causes some preferential orientation and suggests the  $T$ -linear behavior in the  $\beta'$  phase is characteristic of the layers which are likely oriented preferentially with their normal parallel to the pressing direction.

The  $T$ -linear contribution,  $\zeta$ , can be used in conjunction with the Wiedemann-Franz law in order to estimate the electronic component of the thermal conductivity. Using the Sommerfeld Lorentz number of  $2.44 \times 10^{-8} \text{ W}\Omega/\text{K}^2$  we arrive at a value of  $0.23 \text{ W}/(\text{m K})$ . This result is less than previously documented total thermal conductivity [24], which is expected as the total thermal conductivity has both electronic and lattice contributions.

The phase transition temperature acquired via this fit procedure on the resistivity data,  $T_{\beta'}$ , compares well with the phase transition temperature derived from the  $d(\rho)/d(T)$  minimum shown in the inset of Fig. 2(a) suggesting that both methods provide a reasonable assessment of the temperature at which the transition occurs.

From Fig. 6 it is clear that at low temperature the resistivity deviates from quasilinearity and appears to exhibit a  $T^2$  dependence as expected for electron-electron interactions in a Fermi liquid. The inset in Fig. 6 shows a fit to Eq. (8) below 30 K for both warming and cooling curves. The parameters of the fits are given in Table II.

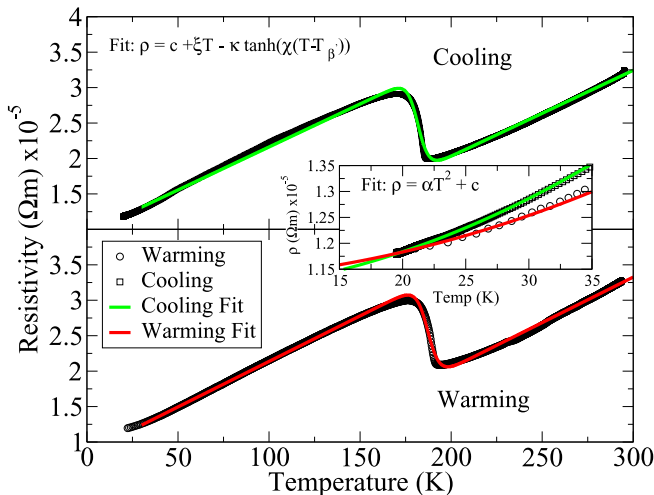


FIG. 6. Experimental dc resistivity compared to a fit to Eq. (7) upon warming (lower panel) and cooling (upper panel). The inset shows the low temperature data compared to a  $T^2$  fit using Eq. (8).

$$\rho = \nu T^2 + C. \quad (8)$$

TABLE II. Resistivity fit parameters acquired by fitting to Eq. (8) at low temperature for both warming and cooling.

Heating direction	$\nu$ ( $\Omega \text{ m} / \text{K}^2 \times 10^{-9}$ )	$C$ ( $\Omega \text{ m} \times 10^{-5}$ )
Cooling	$2.05 \pm 0.02$	$1.10 \pm 0.01$
Warming	$1.41 \pm 0.03$	$1.13 \pm 0.02$

## B. Infrared reflectivity

As seen in Fig. 4 the optical reflectance of  $\beta - \text{As}_2\text{Te}_3$  varies only subtly with temperature, and can be modeled as a simple Drude metal. Only upon transitioning to  $\beta' - \text{As}_2\text{Te}_3$  below  $\approx 190$  K does the material begin to exhibit a more complex reflectivity spectrum characterized by a decrease in the constant reflectance beyond the plasma edge and the appearance of an additional feature, associated with the formation of a pseudogap at the  $\beta$ -to- $\beta'$  phase transition.

### 1. Gapped model

A visualization of the gapped model we used to characterize the pseudogap formation is shown in Fig. 7. Figure 7(a) depicts the Drude conductivity (normalized to 290 K) corresponding to  $\omega_p \approx 6200 \text{ cm}^{-1}$  and  $\Gamma \approx 620 \text{ cm}^{-1}$  (the Drude fit parameters at 85 K) as well as the corresponding fully gapped real optical conductivity with a gap of  $766 \text{ cm}^{-1}$  and broadening of  $39 \text{ cm}^{-1}$  (gapped model fit parameters at 85 K). Figure 7(b) shows the real optical conductivity corresponding to the model fit to our experimental reflectance at 85 K (dashed curve). The ungapped (red curve) and gapped (blue curve) contributions that make up the total real optical conductivity are also depicted. In this example we have a gapping fraction,  $\xi_0$ , of  $\approx 0.25$ .

In this case Eq. (5) is equivalent to

$$\sigma_{\text{gap}}(\omega) = 0.75 \sigma_{\text{Drude}}(\omega) + 0.25 \sigma_G(\omega), \quad (9)$$

where  $\sigma_{\text{Drude}}$  and  $\sigma_G$  are, respectively, the fully ungapped and fully gapped real optical conductivity curves shown in Fig. 7(a).

Physically the gapped model is describing the contributions of three electronic channels: the charge carriers that have been gapped (channel A), those that remain normal (channel B), and those contributing to a sharp mode at the origin (channel C). The channel A carriers do not contribute to the real optical conductivity until enough energy is available for excitation across the gap, and hence contribute no spectral weight below the gapping frequency. This implies that, despite 25% of the carriers participating in channel A, at frequencies above the gap, channel A carriers with enough energy contribute spectral weight. The actual missing spectral weight thus amounts to  $\approx 15\%$  of the total spectral weight of  $\sigma_{\text{Drude}}$  in the region below  $5000 \text{ cm}^{-1}$ . The missing spectral weight is shown in Fig. 7(c) (see below also).

In general, due to the optical sum rule, missing spectral weight must be recovered at either lower or higher energy. In this case, since the low-frequency limit of the real optical conductivity does not match the dc conductivity, we assume that

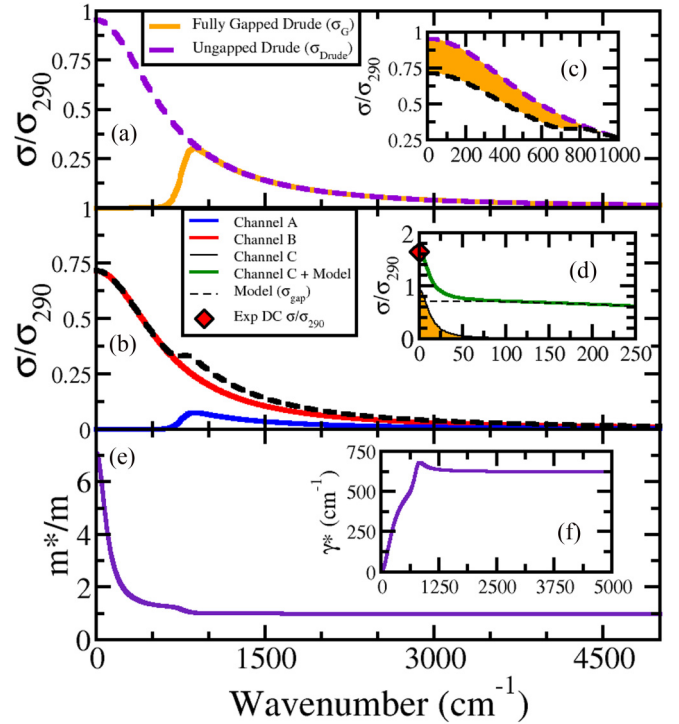


FIG. 7. (a) Example real ungapped ( $\sigma_{\text{Drude}}$ ) and gapped ( $\sigma_G$ ) Drude conductivity. Model parameters are given in the main text. (b) Real optical conductivity ( $\sigma_{\text{gap}}$ ) at 85 K (dashed curve) is comprised of both gapped and ungapped contributions (labeled channel A and channel B, respectively). (c) Shaded region shows the difference spectral weight of our model ( $\sigma_{\text{gap}}$ , lower curve) and a fully ungapped Drude using the same parameters ( $\sigma_{\text{Drude}}$ , upper curve). (d) Missing spectral weight is modeled as a narrow Drude contribution with higher effective mass. See the main text for details. (e) Effective mass and (f) scattering rate as a function of wavenumber from an extended Drude analysis of the partially gapped model whose real optical conductivity is presented as a dashed curve in (b). The horizontal axis of all inset graphs is in  $\text{cm}^{-1}$ .

it goes into a mass-renormalized peak at the origin (channel C) with a scattering width below the experimental spectral range. To estimate its contribution we used the dielectric function from our fit to calculate the frequency-dependent mass and scattering rate according to the extended Drude model [34,44]. This is shown for the 85 K fit in Figs. 7(e) and 7(f) from which we find the effective mass ratio  $m^*/m_e \approx 7$  near the origin. These curves were generated using the values of  $\omega_p$  and  $\epsilon_\infty$  plotted in Fig. 5 derived from the 85 K model fit. The missing spectral weight,  $\Delta A$ , is shown as the shaded region between our real model optical conductivity,  $\sigma_{\text{gap}}(\omega)$ , and the corresponding ungapped real Drude conductivity,  $\sigma_{\text{Drude}}(\omega)$ , in Fig. 7(c) and can be calculated by subtracting the integrated spectral weight of the model from that of the corresponding ungapped Drude model according to

$$\begin{aligned} \Delta A &= \int_0^\infty \sigma_{\text{Drude}}(\omega) d\omega - \int_0^\infty \sigma_{\text{gap}}(\omega) d\omega \\ &= \frac{\omega_p^2}{8} \frac{2\pi c}{9 \times 10^{11}} \frac{m^*}{m_e}. \end{aligned} \quad (10)$$

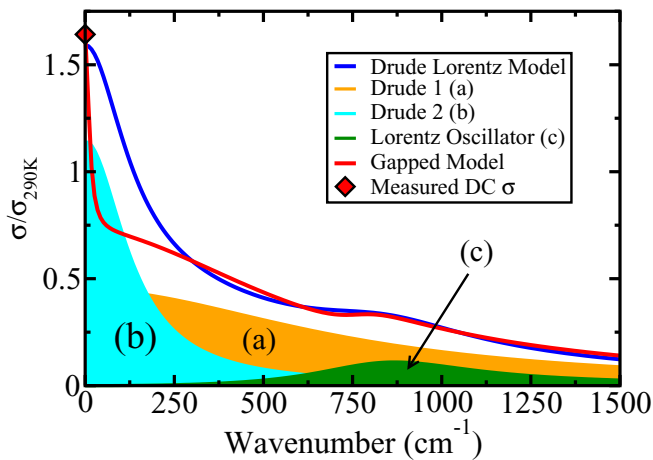


FIG. 8. The 85 K Drude-Lorentz model compared to the gapped model, also at 85 K. The shaded regions (a) and (b) represent the two Drude contributions and (c) represents the Lorentzian contribution to the conductivity. The two models deviate below the effective range of the MIR experiment.

Here  $\omega_p^*$  represents the plasma frequency of the mass renormalized sharp mode (channel C) that, when added to channels A and B, satisfies the optical sum rule and  $2\pi c/9 \times 10^{11}$  is a conversion factor when the optical conductivities are in  $\Omega^{-1} \text{cm}^{-1}$ ,  $\omega_p$  is in  $\text{cm}^{-1}$ , and  $c$ , the speed of light, is in  $\text{cm/s}$ . To match the dc conductivity we found the narrow mode (modeled as a Drude oscillator) has a scattering width of  $12 \text{cm}^{-1}$ , below our experimentally accessible spectral range. The result is shown in Fig. 7(d) where the lower shaded curve shows this mass-renormalized contribution, the dashed curve shows the real model optical conductivity obtained from the fit to the experimental reflectance, and the solid curve shows their sum which matches the dc conductivity in the zero-frequency limit. Note that while the model assumes all of the missing spectral weight is recovered via a narrow oscillator at zero frequency, it is also possible that some moves to higher energies beyond the measurement range, in which case the mass-renormalized zero-frequency oscillator would have less spectral weight, and would be even narrower in order to match with the dc conductivity.

## 2. Comparison to Drude-Lorentz model

Both the gapped model and the Drude-Lorentz model fit the experimental reflectivity curves well in the region of the acquired data and confirm the need for an additional model contribution below the temperature of the phase transition which is attributed to excitation of carriers across a partial gap. The real optical conductivity from the 85 K Drude-Lorentz fit is compared to the gapped model in Fig. 8 with the shaded regions representing the contributions that form the double-Drude + Lorentzian conductivity. Both models are virtually indistinguishable above  $250 \text{cm}^{-1}$ .

As observed in Fig. 8 with the addition of the second Drude term, the Drude-Lorentz model reproduces the expected low temperature real dc conductivity without mass renormalization. However, as seen in Fig. S2 of the Supplemental Material at temperatures in the vicinity of the phase transition the

agreement is poor, with the model overshooting the measured dc conductivity [32]. This is further evident when the measured dc resistivity shown in Fig. 2(a) is compared to the optical resistivity of both models in Figs. 2(b) and 2(c). While the gapped model reproduces the steplike increase at the phase transition, the Drude-Lorentz model does not. The gapped model does not exhibit the expected metallic linear temperature dependence below the phase transition, presumably due to the need to add the narrow mass-renormalized zero-frequency oscillator modeled at low temperature in Fig. 7. To definitively confirm the low-frequency behavior of the optical conductivity, low temperature terahertz spectroscopy is required.

## 3. Proposed pseudogap origin

In addition to the concomitant partial gap formation observed in the optical properties, the similarities in the resistivity signatures at the  $\beta$ - $\beta'$  phase transition in  $\text{As}_2\text{Te}_3$ , and at the CDW transitions in other materials such as  $\text{Er}_2\text{Ir}_3\text{Si}_5$  [42,43],  $\text{Cu}_2\text{Se}$  [45], and  $\text{NbSe}_2$  [6], suggests that the  $\beta$ -to- $\beta'$  transition may be caused by the formation of a charge density wave. In CDW order, periodic modulations of the charge density cause a reorganization of the Fermi surface which lowers the overall energy, leading to the formation of an energy gap, and often an accompanying structural phase transition. Support for this interpretation comes from XRD and neutron scattering measurements that have confirmed that the monoclinic distortion at the  $\beta$ -to- $\beta'$  phase transition is accompanied by a fourfold modulation along the  $b$  axis [16]. Additional experimental evidence for CDW order comes from the hysteresis observed in the dc resistivity. Thermal hysteresis behavior is a common feature of the CDW transition. It is believed to be caused by pinning of the CDW phase to impurities [46]. As a result of the Fermi surface reconstruction different metastable states may occur and thermal history becomes important in determining the properties near the transition. The presence of lattice defects arising from the polycrystalline synthesis of melt-quenched  $\text{As}_2\text{Te}_3$  and the tendency of sesquichalcogenides to have non-negligible antisite doping [29], suggests that pinning of a CDW is a possible explanation for the thermal hysteresis observed in the dc resistivity at the  $\beta$ - $\beta'$  phase transition in  $\text{As}_2\text{Te}_3$ .

Two- and three-dimensional materials that undergo a CDW transition such as the rare-earth ( $R$ ) tritellurides,  $R\text{Te}_3$  [7,8],  $\text{VSe}_2$  [47],  $\eta$ - $\text{Mo}_4\text{O}_{11}$ ,  $\gamma$ - $\text{Mo}_4\text{O}_{11}$  [48], and  $\text{CsV}_3\text{Sb}_5$  [38] remain metallic, due to the opening of only a partial gap on the Fermi surface. The real optical conductivity below the CDW transition generally shows a reorganization of some of the spectral weight into a narrow, Drude-like response and high-frequency tail that deviates from the Drude form and results from single-particle excitations across the gap. Similar to our results for  $\beta' - \text{As}_2\text{Te}_3$ , in  $\text{VSe}_2$  [47],  $\eta$ - $\text{Mo}_4\text{O}_{11}$ , and  $\gamma$ - $\text{Mo}_4\text{O}_{11}$  [48], the dc conductivity is significantly higher than the low-frequency limit of the experimental real optical conductivity at low temperature in the CDW state, and is reconciled via a narrow mode at the origin below the experimental spectral range. It might be tempting to attribute this to a sliding collective mode of the CDW as has been suggested for  $\text{VSe}_2$  [47]; however, the response of the considerable

residual metallic component is expected to screen optically active modes including collective modes. Furthermore, the hysteresis in the dc resistivity of  $\text{As}_2\text{Te}_3$  indicates significant pinning so that the optical reflectance measurement (which invokes an ac as opposed to dc field) is unlikely to induce strong enough electric fields.

## V. CONCLUSIONS

In this work we have investigated the transport and optical properties of melt-quenched  $\text{As}_2\text{Te}_3$  via dc resistivity and optical reflectivity experiments. We implemented a phenomenological fit to analyze the  $\beta$ -to- $\beta'$  phase transition signature in the dc resistivity, and observed slope invariance across this transition. The simple model used has been shown to fit quite well over a wide range of temperatures whilst reasonably reproducing the  $\beta$ -to- $\beta'$  anomaly. The  $T^2$  dependence of the resistivity below approximately 30 K, indicates that electron-electron interactions characteristic of a Fermi liquid dominate at the lowest temperatures despite  $\beta' - \text{As}_2\text{Te}_3$  being a poor metal with high resistivity. Optical measurements suggest that the anomaly accompanying the  $\beta$ -to- $\beta'$  phase

transition in the resistivity is due to the formation of a partial gap of magnitude  $\approx 100$  meV (taking into account the results of both models) on the Fermi surface affecting approximately 25% of the conducting electrons. Based on these observations, and the thermal hysteresis observed in the phase transition in the dc resistivity, we propose that the  $\beta$ -to- $\beta'$  phase transition could be the result of CDW formation. With the observation of low-temperature electronic instability in  $\text{As}_2\text{Te}_3$ , comes the possibility that chemical doping and/or substitution may lead to the emergence of new phenomena allowing further tuning for applications, towards a quantum critical point or a topological insulating state.

## ACKNOWLEDGMENTS

The authors acknowledge valuable discussions with D. A. Crandles and funding support from Brock University and the Natural Sciences and Engineering Research Council of Canada (NSERC). Additional scholarship funding was provided to J.D. from the Ontario Graduate Scholarship Program and to C.T. from the Natural Sciences and Engineering Research Council of Canada (Canada Graduate Scholarship Program).

- 
- [1] M. Čulo, M. Berben, Y.-T. Hsu, J. Ayres, R. D. H. Hinlopen, S. Kasahara, Y. Matsuda, T. Shibauchi, and N. E. Hussey, Putative Hall response of the strange metal component in  $\text{FeSe}_{1-x}\text{S}_x$ , *Phys. Rev. Research* **3**, 023069 (2021).
- [2] G. Grüner, The dynamics of charge-density waves, *Rev. Mod. Phys.* **60**, 1129 (1988).
- [3] D. K. Pratt, M. G. Kim, A. Kreyssig, Y. B. Lee, G. S. Tucker, A. Thaler, W. Tian, J. L. Zarestky, S. L. Bud'ko, P. C. Canfield, B. N. Harmon, A. I. Goldman, and R. J. McQueeney, Incommensurate Spin-Density Wave Order in Electron-Doped  $\text{BaFe}_2\text{As}_2$  Superconductors, *Phys. Rev. Lett.* **106**, 257001 (2011).
- [4] S. Nagata and T. Atake, Survey of chalcogenide superconductors, *J. Therm. Anal. Calorim.* **57**, 807 (1999).
- [5] M. Z. Hasan and J. E. Moore, Three-dimensional topological insulators, *Annu. Rev. Condens. Matter Phys.* **2**, 55 (2011).
- [6] J. Chaussy, P. Haen, J. Lasjaunias, P. Monceau, G. Waysand, A. Waintal, A. Meerschaut, P. Molinié, and J. Rouxel, Phase transitions in  $\text{NbSe}_3$ , *Solid State Commun.* **20**, 759 (1976).
- [7] F. Pfuner, P. Lerch, J.-H. Chu, H.-H. Kuo, I. R. Fisher, and L. Degiorgi, Temperature dependence of the excitation spectrum in the charge-density-wave  $\text{ErTe}_3$  and  $\text{HoTe}_3$  systems, *Phys. Rev. B* **81**, 195110 (2010).
- [8] B. F. Hu, B. Cheng, R. H. Yuan, T. Dong, and N. L. Wang, Coexistence and competition of multiple charge-density-wave orders in rare-earth tritellurides, *Phys. Rev. B* **90**, 085105 (2014).
- [9] K. Yumigeta, Y. Qin, H. Li, M. Blei, Y. Attarde, C. Kopas, and S. Tongay, Advances in rare-earth tritelluride quantum materials: Structure, properties, and synthesis, *Adv. Sci.* **8**, 2004762 (2021).
- [10] Y. Cheng, O. Cojocaru-Mirédin, J. Keutgen, Y. Yu, M. Küpers, M. Schumacher, P. Golub, J.-Y. Raty, R. Dronskowski, and M. Wuttig, Understanding the structure and properties of sesquichalcogenides (i.e.,  $\text{V}_2\text{VI}_3$  or  $\text{Pn}_2\text{Ch}_3$  (Pn = pnictogen, Ch = chalcogen) compounds) from a bonding perspective, *Adv. Mater.* **31**, 1904316 (2019).
- [11] S. Buga, V. Kulbachinskii, V. Kytin, G. Kytin, I. Kruglov, N. Lvova, N. Perov, N. Serebryanaya, S. Tarelkin, and V. Blank, Superconductivity in bulk polycrystalline metastable phases of  $\text{Sb}_2\text{Te}_3$  and  $\text{Bi}_2\text{Te}_3$  quenched after high-pressure-high-temperature treatment, *Chem. Phys. Lett.* **631-632**, 97 (2015).
- [12] J. L. Zhang, S. J. Zhang, H. M. Weng, W. Zhang, L. X. Yang, Q. Q. Liu, S. M. Feng, X. C. Wang, R. C. Yu, L. Z. Cao, L. Wang, W. G. Yang, H. Z. Liu, W. Y. Zhao, S. C. Zhang, X. Dai, Z. Fang, and C. Q. Jin, Pressure-induced superconductivity in topological parent compound  $\text{Bi}_2\text{Te}_3$ , *Proc. Natl. Acad. Sci. USA* **108**, 24 (2011).
- [13] J. Zhang, S. Zhang, P. Kong, J. Zhu, X. Li, J. Liu, L. Cao, and C. Jin, Superconductivity in copper intercalated topological compound  $\text{Cu}_x\text{Bi}_2\text{Te}_3$  induced via high pressure, *Phys. C (Amsterdam, Neth.)* **493**, 75 (2013).
- [14] J. Manson, A. Madubuonu, D. A. Crandles, C. Uher, and P. Loš'ták, Infrared spectroscopy of Cr- and V-doped  $\text{Sb}_2\text{Te}_3$ : Dilute magnetic semiconductors, *Phys. Rev. B* **90**, 205205 (2014).
- [15] J. S. Dyck, Č. Drašar, P. Lošt'ák, and C. Uher, Low-temperature ferromagnetic properties of the diluted magnetic semiconductor  $\text{Sb}_{2-x}\text{Cr}_x\text{Te}_3$ , *Phys. Rev. B* **71**, 115214 (2005).
- [16] C. Morin, S. Corallini, J. Carreaud, J.-B. Vaney, G. Delaizir, J.-C. Crivello, E. B. Lopes, A. Piarristeguy, J. Monnier, C. Candolfi, V. Nassif, G. J. Cuello, A. Pradel, A. P. Goncalves, B. Lenoir, and E. Alleno, Polymorphism in thermoelectric  $\text{As}_2\text{Te}_3$ , *Inorg. Chem.* **54**, 9936 (2015).



- [17] N. S. Platakis, Phase transitions and electrical properties of  $\text{As}_2\text{Te}_3$ , *J. Non-Cryst. Solids* **24**, 365 (1977).
- [18] J.-B. Vaney, J. Carreaud, G. Delaizir, C. Morin, J. Monnier, E. Alleno, A. Piarristeguy, A. Pradel, A. Pereira Goncalves, E. Lopes, C. Candolfi, A. Dauscher, and B. Lenoir, Low-temperature transport properties of bi-substituted  $\beta - \text{As}_2\text{Te}_3$  compounds, *J. Electron. Mater.* **45**, 1786 (2015).
- [19] J.-B. Vaney, J. Carreaud, A. Piarristeguy, C. Morin, G. Delaizir, R. Viennois, M. Colas, J. Cornette, E. Alleno, J. Monnier, M. Bigot, A. P. Gonçalves, E. B. Lopes, G. J. Cuello, V. Nassif, C. Candolfi, B. Lenoir, and A. Pradel, Stabilization of metastable thermoelectric crystalline phases by tuning the glass composition in the Cu-As-Te system, *Inorg. Chem.* **57**, 754 (2018).
- [20] J.-B. Vaney, J. Carreaud, G. Delaizir, A. Pradel, A. Piarristeguy, C. Morin, E. Alleno, J. Monnier, A. P. Gonçalves, C. Candolfi, A. Dauscher, and B. Lenoir, High-temperature thermoelectric properties of Sn-doped  $\beta - \text{As}_2\text{Te}_3$ , *Adv. Electron. Mater.* **1**, 1400008 (2015).
- [21] K. Pal and U. V. Waghmare, Strain induced Z2 topological insulating state of  $\beta - \text{As}_2\text{Te}_3$ , *Appl. Phys. Lett.* **105**, 062105 (2014).
- [22] T. K. Reid, S. K. Nayak, and S. P. Alpay, Strain-induced surface modalities in pnictogen chalcogenide topological insulators, *J. Appl. Phys.* **129**, 015304 (2021).
- [23] E. L. da Silva, A. Leonardo, T. Yang, M. C. Santos, R. Vilaplana, S. Gallego-Parra, A. Bergara, and F. J. Manjón,  $\beta\text{-As}_2\text{Te}_3$ : Pressure-induced three-dimensional Dirac semimetal with ultralow room-pressure lattice thermal conductivity, *Phys. Rev. B* **104**, 024103 (2021).
- [24] J.-B. Vaney, J.-C. Crivello, C. Morin, G. Delaizir, J. Carreaud, A. Piarristeguy, J. Monnier, E. Alleno, A. Pradel, E. Lopes, A. Pereira Goncalves, A. Dauscher, C. Candolfi, and B. Lenoir, Electronic structure, low-temperature transport and thermodynamic properties of polymorphic  $\beta - \text{As}_2\text{Te}_3$ , *RSC Adv.* **6**, 52048 (2016).
- [25] A. Vaitkus, A. Merkys, and S. Gražulis, Validation of the crystallography open database using the crystallographic information framework, *J. Appl. Crystallogr.* **54**, 661 (2021).
- [26] A. Bradley, The crystal structure of tellurium, *Philos. Mag. (1798-1977)* **48**, 477 (1924).
- [27] L. J. van der Pauw, A method of measuring specific resistivity and Hall effect of discs of arbitrary shape, *Philips Res. Rep.* **13**, 1 (1958).
- [28] C. C. Homes, M. Reedyk, D. Cradles, and T. Timusk, Technique for measuring the reflectance of irregular, submillimeter-sized samples, *Appl. Opt.* **32**, 2976 (1993).
- [29] T. Zhu, L. Hu, X. Zhao, and J. He, New insights into intrinsic point defects in  $\text{V}_2\text{VI}_3$  thermoelectric materials, *Adv. Sci.* **3**, 1600004 (2016).
- [30] K. Matsubayashi, T. Terai, J. S. Zhou, and Y. Uwatoko, Superconductivity in the topological insulator  $\text{Bi}_2\text{Te}_3$  under hydrostatic pressure, *Phys. Rev. B* **90**, 125126 (2014).
- [31] G. S. Hegde, A. Prabhu, C. Yang, and Y. Kuo, Reduction in electrical resistivity of bismuth selenide single crystal via Sn and Te co-doping, *Mater. Chem. Phys.* **278**, 125675 (2022).
- [32] See Supplemental Material at <http://link.aps.org/supplemental/10.1103/PhysRevB.106.075104> for a more in-depth analysis of the reflectance data and modeling.
- [33] A. B. Kuzmenko, Kramers-Kronig constrained variational analysis of optical spectra, *Rev. Sci. Instrum.* **76**, 083108 (2005).
- [34] A. Kuzmenko, Guide to RefFIT: Software to fit optical spectra, version 1.3.04 (2016), <https://reffit.ch/wp-content/uploads/2018/10/Manual.pdf>.
- [35] C. Homes, T. Timusk, D. Bonn, R. Liang, and W. Hardy, Optical properties along the  $c$ -axis of  $\text{YBa}_2\text{Cu}_3\text{O}_{6+x}$ , for  $x = 0.50 \rightarrow 0.95$  evolution of the pseudogap, *Phys. C (Amsterdam, Neth.)* **254**, 265 (1995).
- [36] V. Vescoli, L. Degiorgi, H. Berger, and L. Forro, The optical properties of the correlated two-dimensional  $2\text{H-TaSe}_2$  system, *Synth. Met.* **103**, 2655 (1999).
- [37] X. B. Wang, H. P. Wang, H. Wang, M. Fang, and N. L. Wang, Optical properties of  $\text{TlNi}_2\text{Se}_2$ : Observation of pseudogap formation, *Phys. Rev. B* **92**, 245129 (2015).
- [38] X. Zhou, Y. Li, X. Fan, J. Hao, Y. Dai, Z. Wang, Y. Yao, and H.-H. Wen, Origin of the charge density wave in the kagome metal  $\text{CsV}_3\text{Sb}_5$  as revealed by optical spectroscopy, *Phys. Rev. B* **104**, L041101 (2021).
- [39] N. Ni, S. Nandi, A. Kreyssig, A. I. Goldman, E. D. Mun, S. L. Bud'ko, and P. C. Canfield, First-order structural phase transition in  $\text{CaFe}_2\text{As}_2$ , *Phys. Rev. B* **78**, 014523 (2008).
- [40] A. Kiswandhi, J. S. Brooks, H. B. Cao, J. Q. Yan, D. Mandrus, Z. Jiang, and H. D. Zhou, Competition between the structural phase transition and superconductivity in  $\text{Ir}_{1-x}\text{Pt}_x\text{Te}_2$  as revealed by pressure effects, *Phys. Rev. B* **87**, 121107(R) (2013).
- [41] Y. Singh, D. Pal, S. Ramakrishnan, A. M. Awasthi, and S. K. Malik, Phase transitions in  $\text{Lu}_2\text{Ir}_3\text{Si}_5$ , *Phys. Rev. B* **71**, 045109 (2005).
- [42] S. Ramakrishnan, A. Schönleber, T. Rekiş, N. van Well, L. Noohinejad, S. van Smaalen, M. Tolkiel, C. Paulmann, B. Bag, A. Thamizhavel, D. Pal, and S. Ramakrishnan, Unusual charge density wave transition and absence of magnetic ordering in  $\text{Er}_2\text{Ir}_3\text{Si}_5$ , *Phys. Rev. B* **101**, 060101 (2020).
- [43] P. Lalngilneia, A. Thamizhavel, and S. Ramakrishnan, Coupling of rare earth moment and charge density wave ordering in a single crystal  $\text{Er}_2\text{Ir}_3\text{Si}_5$ , *J. Phys.: Conf. Ser.* **592**, 012094 (2015).
- [44] D. B. Tanner, *Optical Effects in Solids* (Cambridge University Press, Cambridge, UK, 2019).
- [45] M. Yao, W. Liu, X. Chen, Z. Ren, S. Wilson, Z. Ren, and C. Opeil, Anomalous CDW ground state in  $\text{Cu}_2\text{Se}$ : A wave-like fluctuation of  $dc$  I-V curve near 50 k, *J. Materiomics* **3**, 150 (2014).
- [46] C. S. Lue, Y.-K. Kuo, F. H. Hsu, H. H. Li, H. D. Yang, P. S. Fodor, and L. E. Wenger, Thermal hysteresis in the charge-density-wave transition of  $\text{Lu}_5\text{Rh}_4\text{Si}_{10}$ , *Phys. Rev. B* **66**, 033101 (2002).
- [47] X. Feng, J. Henke, C. Morice, C. J. Sayers, E. Da Como, J. van Wezel, and E. van Heumen, Signatures of the charge density wave collective mode in the infrared optical response of  $\text{VSe}_2$ , *Phys. Rev. B* **104**, 165134 (2021).
- [48] A. W. McConnell, B. P. Clayman, C. C. Homes, M. Inoue, and H. Negishi, Polarized reflectance measurements of the CDW transitions in  $\eta\text{-Mo}_4\text{O}_{11}$  and  $\gamma\text{-Mo}_4\text{O}_{11}$ , *Phys. Rev. B* **58**, 13565 (1998).